Energy 225 (2021) 120203

Contents lists available at ScienceDirect

Energy

journal homepage: www.elsevier.com/locate/energy

Hydro-mechanical-chemical modeling of sub-nanopore capillary-confinement on CO_2-CCUS-EOR

Mingyu Cai [a, b, 1], Yuliang Su [a, 2, *], Derek Elsworth [b, 3], Lei Li [a, 4], Liyao Fan [a, 2]

[a] Key Laboratory of Unconventional Oil & Gas Development (China University of Petroleum (East China)), Ministry of Education, Qingdao, 266580, PR China
[b] Energy and Mineral Engineering & Geosciences, The Pennsylvania State University, 110 Hosler Building, University Park, PA, 16802, USA

ARTICLE INFO

Article history:
Received 27 July 2020
Received in revised form
17 February 2021
Accepted 20 February 2021
Available online 1 March 2021

Keywords:
Subnanopore confinement
VLE calculation
CO2 utilization and storage
Compositional simulation
Coupled geomechanics
Tight reservoir

ABSTRACT

Nanopore/subnanopore networks comprising tight reservoirs exhibit special behaviors in the storage and transport of capillary-confined fluids. We develop a hydro-mechanical-chemical model coupling the response of capillary-confined phase behavior, multicomponent flow, reservoir deformation and reaction-controlled porosity evolution to explore the effect of nanopore confinement on enhanced oil recovery and CO_2 storage. The results reveal that confinement effects change both in chemical potential and isothermal compressibility of individual components and thus increases volume expansion for any given pressure drop. For constrained mixtures, the CO_2 K-value (at fixed pressure) and the MMP(at fixed aperture) will shift to smaller than the bulk state. Moreover, capillary-confinement causes an increased production of heavier components when reservoir pressure is below MMP and a higher production of all components and a smaller reservoir inflation when reservoir pressure is higher than MMP - where miscibility dominates. Meanwhile, capillary-confinement causes a slight increase in CO_2 retention rate in the calculation for two cases of native oils with contrasting light oil fractions but in identical reservoirs. Thus any production strategy for a combined CO_2 capture and storage (CCS) operation needs to be formulated in full consideration of the rock and fluid properties for each potential site.

1. Introduction

To meet an increasing energy demand, unconventional hydrocarbon resources, especially tight oil with ultra-low in-situ permeabilities in the range 0.001mD (1μD) to 0.1mD (100μD), have attracted increasing attention [1,2]. Due to both ultra-small pore diameters and exacerbated by poor connectivity, fluid transmission does not follow Darcy's Law – providing significant challenges in flow characterization and fluids recovery [3]. Whether miscible or immiscible, CO_2 injection into tight reservoirs can significantly improve oil recovery [4,5]. Concurrent with the expanding utilization of hydrocarbon fuels, global CO_2 emissions continue to increase – with carbon capture and storage (CCS) widely accepted as a viable method to reduce carbon emissions their impact [6–8]. The closest-to-market and commercially viable way to deploy CCS on a large scale is combined with EOR technology. Such operations enable CO_2 utilization and storage (CCUS) to progress as a viable carbon management strategy where costs are offset by hydrocarbon production [9–14].

Injected CO_2 and the native hydrocarbons repeatedly contact and reach local phase equilibrium within nanopores with the entire process affected by the interaction between pore surface and fluid molecules. When the pore radius is reduced to nanometer scale - comparable to molecular span - fluid-confinement effects are greatly enhanced and fluid phase properties are dramatically impacted [15–18]. Phase behavior of fluids confined in sub-nanopores - which we call confined fluids - is described at a variety of levels complexity involving equations of state and interaction with solid media (Kelvin equation) for continuum models and using density functional theory and molecular simulation at the atomistic scale. Laboratory measurements are particularly challenging due to the complexity of the mixtures, necessarily high pressures and

* Corresponding author.
E-mail addresses: cmymingy@gmail.com (M. Cai), suyuliang@upc.edu.cn (Y. Su).
[1] Postal address: Changjiang West Road 66, Economic Technical Development Zone, Qingdao, Shandong Province, 266580, P.R. China / 209 Academic Project, University Park, PA 16802, United States
[2] Postal address: Changjiang West Road 66, Economic Technical Development Zone, Qingdao, Shandong Province, 266580, P.R. China
[3] Postal address: 110 Hosler Building, University Park, PA 16802, United States
[4] Postal address: Changjiang West Road 66, Economic Technical Development Zone, Qingdao, Shandong Province, 266580, P.R. China

https://doi.org/10.1016/j.energy.2021.120203
0360-5442/

temperatures and needs for high accuracy in observation/imaging systems [19,20]. Driven by these constraints, the slightly oversimplified physical assumptions accommodated in the cubic EOS approach are generally considered acceptable and provide an appropriate method for calculating the phase behavior of confined fluids. The change in critical properties results in the phase behavior of oil and gas in tight reservoirs significantly shifting [21–23]. Another particularly noteworthy example of this difference is the phenomenon commonly seen in nanoscale porous media known as capillary condensation – describing the condensation of trapped fluids below their bulk vapor saturation points [24]. Combining the capillary condensation effect with the Cubic Peng-Robinson equation of state (PR-EOS), the fluid phase behavior in nanopores in tight reservoirs may be dynamically represented [25]. This method has been widely used to improve the numerical simulation of field scale problems, such as shale gas development and CO_2 huff-n-puff recovery [26–29]. However, the simulation of multi-component systems usually involves knowable changes in reservoir temperatures, pressures, and various physical properties of the reservoir or injectate but typically lacks details of native oil composition and characteristics [30]. This shortfall intrinsically results in a limitation on robust predictions of behavior since the adsorption properties and density distributions of light and heavy hydrocarbons under capillary(nano)-confinement vary significantly as pressure decreases [31] – indicating that a separate and detailed analysis of oil composition is necessary. This study compares the phase behavior of different crude oils and CO_2 that would affect both the evolution of reservoir pressure and the production of both lighter and heavier components, thus significantly affecting production strategies.

However, in order to simulate the CCUS process in tight reservoirs more accurately, it is also necessary to consider geomechanical impacts from CO_2 injection and oil production, as well as the dynamic chemical interactions between injected CO_2 and reservoir minerals. The stress state in the reservoir is controlled by pore pressure change during production or injection [30,32,33]. Besides, injected fluids may promote creep through dissolution reactions that enhance microcrack formation and diffusive mass transfer processes, resulting in reservoir deformation that varies over time and that changes the porosity and permeability of the host [34,35]. Prior studies of the kinetics of CO_2-brine-rock reactions [36–39] and saline injection have identified significant increases in reservoir permeability [40]. However, concurrent precipitation and dissolution of secondary minerals such as kaolinite, muscovite, and montmorillonite also impact permeability and are mass flow rate and activity-dependent [41–43].

Most large-scale simulations of CO_2 storage are focused on CO_2 injection into saline aquifers [44] or into shale to interact with methane or single component crude oils [45] including the adsorption and replacement of CO_2 and methane in nanopores at a molecular level [46,47]. However, these approaches intrinsically neglect the complex and important interaction between CO_2 and multi-component mobile liquid hydrocarbons. Furthermore, molecular simulations enable the calculation of the EOS phase behavior of CO_2, nitrogen, and alkanes in nanopores, and then the analysis of the feasibility and optimization for CO_2 storage in tight/shale reservoirs [25]. And indeed, some CO_2-EOR studies have attempted to incorporate these micro-scale migration mechanisms into large-scale flow simulations by expanding the capability of compositional simulators, such as UTCOMP [48] and MSflow-COM [30]. However, current understanding of CO_2 sequestration with multi-component flow under the combined influence of geomechanics and geochemistry remain limited. Approaches using CMG, for example *Fakcharoenphol* et al. [49] and *Chen* et al. [50], have simulated thermo-hydro-mechanical-chemical coupling effects but these approaches are difficult to expand to micromechanical processes at pore-scale. As a result, there is a dearth of work combining phase behavior in nanopores with geomechanics/geochemistry to simulate CO_2 capture and assess storage safety – an essential requirement for successful deployment of CCUS in deep reservoirs.

In this context, we analyze nanopores' influence on fluid phase behavior and CO_2 miscible displacement by establishing rigorous compositional models coupled with geomechanics to evaluate CO_2-CCUS injection processes. The petrophysical characteristics of the fluid and reservoir are from the Changqing tight oil reservoir in China. The pore size distribution and mineral composition of core samples are determined by nuclear magnetic resonance (NMR) and X-ray diffraction (XRD). A Gibbs free energy minimization criterion is applied to modify the PR-EOS, and the vapor-liquid fugacity is calculated by considering the change of criticalities and capillary pressure effect, to study and characterize phase equilibrium. The minimum miscible pressure (MMP) of the CO_2-hydracarbon mixture under subnanopore confinement is calculated by conducting cell-to-cell simulations based on the modified PR-EOS. Deformation–diffusion processes are accommodated within the framework of Biot poroelasticity and the effect of chemical reactions between the injected CO_2 and the native rock is simulated by applying a time-varying porosity equation, related to mineral composition. A field scale study evaluates response to injection and production from vertical wells for the recovery of different hydrocarbon components resulting from the injection of CO_2, including the impacts of reservoir inflation and related permeability change.

2. Experimental materials and methods

2.1. Pore size distribution

The core samples are obtained from wells penetrating four blocks of a tight oil reservoir in Changqing, China. Samples 1 and 2 are recovered from the Chang7 layer, and samples 3 and 4 from Chang8 layer. Detailed parameters defining the core samples are presented in Table 1. These include diameter, d_s, Klinkenberg-corrected permeability, k_∞, and porosity, φ_s, of core samples. Macromr12-110h-i and PoreMaster 60 instruments are used to determine the pore size distribution via NMR spectroscopy and mercury intrusion porosimetry (MIP). MIP experiments are conducted according to the Chinese Oil and Gas Industry Standard SY/T 5346–2010. The maximum operating pressure of the instrument is 60,000psi, measuring pore diameters to 3.564 nm. The experiments are carried out at room temperature (~25 °C).

The advantage of NMR spectroscopy is that the sample's porosity and pore size distribution are not affected by the skeletal composition. Robust correlations are available to link NMR T_2 spectra to MIP data, with this used in this study to convert T_2 spectra into maps of the distribution of pore radii [44,51]. The NMR measurements are recovered from water-saturated core samples and analyzed according to the Chinese Oil and Gas Industry Standard SY/T 6490–2014. The experimental results are presented in Section 4.1.

Table 1
Core sample parameters.

Core No.	Layer	d_s (mm)	k_∞ (mD)	φ_s (%)
Sample 1	Chang 7_2	25.24	0.0268	9.57
Sample 2	Chang 7_2	25.30	0.0131	8.35
Sample 3	Chang 8_1	25.10	3.6904	19.26
Sample 4	Chang 8_2	25.24	0.0300	12.85

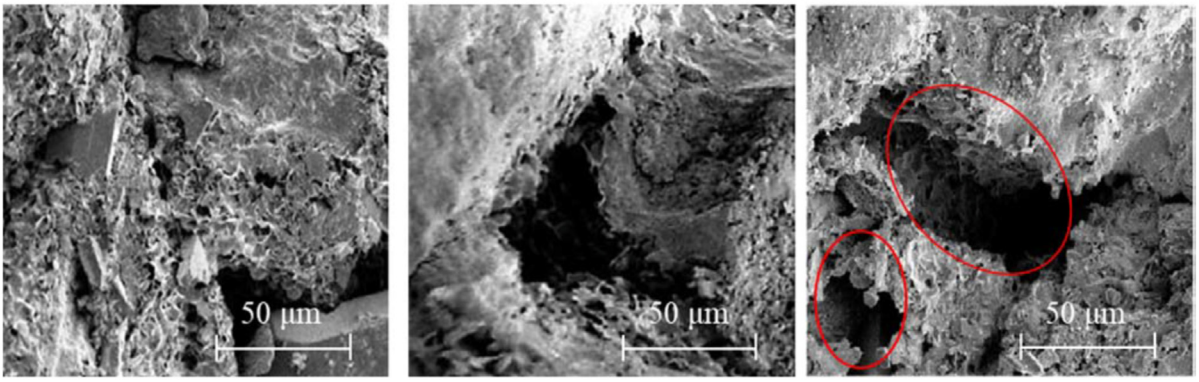

Fig. 1. SEM images of core sample 1.

2.2. Mineral compositions

Potential reactions between supercritical CO_2 and formation water will lead to changes in porosity, injectivity, CO_2 migration and water chemistry [89]. Fig. 1 shows SEM images for core Sample 1 after reacting with CO_2 for 0, 5, and 10 days and illustrating the deposition or reaction products and pore morphology and cementation changes. Such chemical reactions are significantly influenced by key lithologies and mineral compositions [52].

A D/max-2600 X-ray powder diffractometer is used to measure the rock samples' mineral composition in this work. The core samples are powdered to a particle size <40 μm and screened into particles less than #200 mesh. The mineral composition is recovered from the characteristic peaks obtained by XRD. A series of extraction steps isolate clay minerals and aid in the preferred orientation of clay minerals for X-ray analysis. Particles <2 μm are separated by settling in water, with the concentrated paste collected and air-dried. According to the Chinese Oil and Gas Industry Standard SY/T 5163−2010, the mineral compositions are calculated from the XRD results and then incorporated into an analytical solution (Eq.(22)) to describe the evolution of porosity with time. This evaluation identifies the effects of chemical reactions during CO_2 geological storage and its impact on field response. See Section 4.1, following, for mineral compositions and parameters and further discussion of this porosity evolution model.

3. Model and methodology

3.1. Vapor/liquid equilibrium under subnanopore confinement

Two key features controlling fluid state in reservoirs are the significance of critical point transfer and capillary force. This may be achieved by adding capillary forces to the fugacity equation or adjusting key EOS parameters [16,53]. Capillary pressure is calculated in this paper at the porous medium's mean pore size based on the Young-Laplace equation. The initial, undeformed pore radius is obtained from mercury injection porosimetry. We assume that the pores are spherical and that pore radius is updated at each effective pore pressure in the subsequent simulation. The following are satisfied at liquid/vapor equilibrium:

$$P_v - P_L = P_{cap} = \frac{2\sigma co\theta}{r} \tag{1}$$

$$\sigma = \left[\sum_{i}^{N_c} (\overline{\rho}^L [P]_i x_i - \overline{\rho}^V [P]_i y_i)\right]^4 \tag{2}$$

where P_L and P_V are liquid and vapor phase pressures; r is the pore radius; $\overline{\rho}^L$ is the average density of bulk liquid phase; $\overline{\rho}^V$ is the average density of bulk vapor phases; $[P]_i$ is the parachor and the subscript refers to the i-component.

The concept of Gibbs molar free energy is applied to define the vapor-liquid equilibrium (VLE) condition. The system reaches equilibrium when the fugacity of each component across a liquid/vapor interface becomes equal.

$$f_L^i(T, P_L, x) = f_V^i(T, P_V, y), i = 1, \cdots, N_c \tag{3}$$

$$f_L^i(T, P_L, x) = \varnothing_{iL} x_i P_L \tag{4}$$

$$f_V^i(T, P_V, y) = \varnothing_{iV} y_i P_V \tag{5}$$

where f_L^i , f_V^i are liquid and vapor fugacity of the i^{th}-component; x_i and y_i are liquid and vapor phase mole fractions of the i^{th}-component in equilibrium at a given pressure and temperature; $\varnothing_{iL}$ and $\varnothing_{iV}$ are the fugacity coefficients of the i^{th}-component in the liquid and vapor phases. Then we can reformulate the VLE via the K-value according to Eq. (6) [29,54].

$$K_i' = \frac{y_i}{x_i} = \frac{\varnothing_{iL} P_L}{\varnothing_{iV} P_V} = K_i \frac{P_L}{P_V} \tag{6}$$

where K_i and K_i' are the K-values before and after correction by capillary pressure.

Confined spaces or pores alter the phase behavior of fluids, and these effects have been documented in altering critical properties. *Zarragoicoechea and Kuz* et al. [55] used a van der Waals model to simulate the reduction of critical temperature in nanopores, with a quadratic correlation between the change in critical properties and the Lennard-Jones collision diameter ratio to pore throat radius. However, the estimation of critical properties for heavy hydrocarbon components ($C_{22\text{-}80}$) in very small pore spaces (<3 nm) fall outside the range of experimental data [56]. *Singh* et al. [57] reported the variation of critical temperature and pressure of alkanes in slit pores with a width of 0.5−5 nm by using the Grand Canonical Monte Carlo (GCMC) method, with the results similar to those of

the *Zarragoicoechea and Kuz* [55] simulation. Based on the *Singh* [57] data, *Devegowda* et al. [58] fitted equations to calculate the critical properties of C_1, nC_4, and nC_8 in pores respectively 2, 4, and 5 nm in diameter. *Ma* et al. [59] established a consistent model of C_1, nC_4, and nC_8 criticalities in a confined space of dimension 2–10 nm, which is more applicable to the mixed phase behavior consistent with multi-component coexistence. The shifted critical properties can be calculated as [28,60]:

$$\Delta T_c = \frac{T_{cb} - T_{cp}}{T_{cb}} = 1.1775\left(\frac{d_p}{\sigma_{eff}}\right)^{-1.338} for\left(\frac{d_p}{\sigma_{eff}}\right) \geq 1.5 \tag{7}$$

$$\Delta T_c = \frac{T_{cb} - T_{cp}}{T_{cb}} = 0.6 for\left(\frac{d_p}{\sigma_{eff}}\right) < 1.5 \tag{8}$$

$$\Delta P_c = \frac{P_{cb} - P_{cp}}{P_{cb}} = 1.5686\left(\frac{d_p}{\sigma_{eff}}\right)^{-0.783} \tag{9}$$

where σ_{eff} is the effective molecular diameter; d_p is pore diameter.

3.2. Minimum miscible pressure calculation

Traditional cell-to-cell simulation is applied to reproduce the phase behavior with a multi-stage contact between gas and oil. The calculation steps are as follows [61,62]:

(1) First, CO_2 is mixed with the original oil at different molar ratios and the increment ratio of CO_2 and oil is set as 5%. Flash calculations are then performed for the mixtures to detect the two-phase region. If no two-phase region is encountered, the process is judged to be the first contact miscibility and the calculation stops. Otherwise, the calculation proceeds to Steps 2 and 3.
(2) The first point (5% CO_2) of the two-phase region detected in the first step is treated to remove all liquid from the system. The remaining gas is combined with the original oil and the gas-oil at a ratio of 10%. The procedure of the flash calculation is repeated and the liquid removed. This simulates the evaporation or extraction process.
(3) Again, the first point (5% CO_2) of the two-phase region detected in the first step is treated to remove all vapor from the system. The remaining liquid is combined with the CO_2 at a ratio of 10%. The flash calculation repeated and the vapor removed until the oil cannot be further enriched. This simulates the condensate gas drive process.

3.3. Coupled geomechanical and geochemical modeling

The high heterogeneity of the reservoir and the complexity of the fluid-rock interactions provide a challenge in building large-scale models to simulate fluid flow and mechanical deformation in underground geological structures. The simulation's fidelity is critical for the correct prediction of underground hydrodynamics and geomechanics (stress and deformation) and the safety assessment of engineering applications such as hydrocarbon and geothermal yields [63–66].

Fluid flow and deformation of porous media result from changes in fluid pressure or stress state. The continuity equation fluid transmission can be written as [67,68]:

$$\frac{\partial\left(\rho_f \varphi\right)}{\partial t} + \nabla \cdot \left(\rho_f \varphi \vec{v}_f\right) = f_f \tag{10}$$

where ρ_f is the average fluid density that can be obtained from the modified PR-EOS; φ is the porosity; f_f is the source or sink term; $\vec{v}_f$ is the fluid velocity related to specific discharge, $\vec{q}$, through Darcy's law as:

$$\vec{q} = \varphi\left(\vec{v}_f - \vec{v}_s\right) = -\frac{k}{\mu}\nabla P \tag{11}$$

$$\vec{v}_s = \frac{\partial \varepsilon_v}{\partial t} \tag{12}$$

where $\vec{v}_s$ is the solid grain velocity; k is reservoir intrinsic permeability; μ is the dynamic viscosity; P is the fluid pressure perturbation; and ε_v is the volumetric strain of the porous medium.

Substituting Eqs. (11) and (12) into Eq. (10) and expanding gives:

$$\rho_f \frac{\partial \varphi}{\partial t} + \varphi \frac{\partial \rho_f}{\partial P}\frac{\partial P}{\partial t} + \rho_f \varphi \frac{\partial \varepsilon_v}{\partial t} + \nabla \cdot \left(\rho_f \vec{q}\right) = f_f \tag{13}$$

The rate of change of porosity is related to changes in pressure and strain and can be given as [67]:

$$\frac{\partial \varphi}{\partial t} = (\alpha - \varphi)\left(\frac{1}{K_s}\frac{\partial P}{\partial t} + \frac{\partial \varepsilon_v}{\partial t}\right) \tag{14}$$

where K_s is the bulk modulus of the solid rock grains; and α is the Biot effective stress coefficient. It should be noted that the pore relationship here is based on poroelasticity and does not account for the effects of reservoir damage [69]. Substituting Eq. (14) into Eq. (13) yields the following:

$$\left[(\alpha - \varphi)\frac{\rho_f}{K_s} + \varphi \frac{\partial \rho_f}{\partial P}\right]\frac{\partial P}{\partial t} + \rho_f(\alpha - \varphi)\frac{\partial \varepsilon_v}{\partial t} + \nabla \cdot \left(\rho_f \vec{q}\right) = f_f. \tag{15}$$

The equation for mechanical equilibrium is given as,

$$\nabla \sigma = \vec{0} \tag{16}$$

where the effective stress, σ', is given by Biot's general definition as,

$$\sigma = \sigma' + \alpha p \boldsymbol{I} \tag{17}$$

where this may be substituted into the linear constitutive model representing stress-strain as,

$$\sigma' = -2G\varepsilon - \left(K - \frac{2}{3}G\right)\varepsilon_v \boldsymbol{I} \tag{18}$$

where σ is the total stress tensor; $\boldsymbol{I}$ is the second rank identity tensor; ε is the strain tensor; G is the shear modulus; and K is the bulk modulus.

Strains, ε, are related to solid displacements, $\vec{u}$, as,

$$\varepsilon = \frac{1}{2}\left[\nabla \vec{u} + (\nabla \vec{u})^T\right] \tag{19}$$

with the volumetric strain,ε_v , defined as,

$$\varepsilon_v = \nabla \vec{u} = tr(\varepsilon). \tag{20}$$

Integrating Eq. (14) and then substituting Eq. (20) produces the

porosity relationship

$$\varphi - \varphi_0 = \alpha \nabla \vec{u} + \frac{\alpha - \varphi_0}{K_s}(P - P_0) \tag{21}$$

where φ_0 and P_0 are the initial state of porosity and fluid pressure, respectively.

The formation or removal of scale on the pore surface due to precipitation or dissolution may also change porosity — but by mechanisms that add mass to the system, rather the inert deformations represented in Eq. (21). These will result in additional porosity and permeability changes, thus affecting the transport rate of various porous media. Thus, we represent the interaction between CO_2 and the native rock to accommodate the impacts of mineral reaction modulated by mineral composition. This model neglects the calculation of changes in reactant concentration to improve operational efficiency.

Fluid paths in the porous medium change continuously as immobile sediments are formed in, or removed from, the pore space, thus adapting to the path of least resistance under existing conditions. Specific flow path changes can only be determined by network modeling. Although more instructive, this detailed internal flow in a complex and changing porous structure can be tedious and computationally demanding [70]. *Civan* et al. [71] provided a practical analytical solution to describe scale precipitation and dissolution kinetics on the pore surface based on fractal attributes of the pores (see Eq. (22))

$$\varphi_c = \varphi_0 \left(1 + k_\varphi \varphi_0^{r_l} t\right)^{-1/r_l} \tag{22}$$

$$r_l = mD/3 \tag{23}$$

$$k_\varphi = k_m (F_s - 1) C^m n^{m - r_l} V_b^{r_l} \tag{24}$$

$$k_m = k_{m25} exp\left[\frac{-E_a}{R}\left(\frac{1}{T} - \frac{1}{298}\right)\right] \tag{25}$$

where φ_c is the porosity affected by dissolution/precipitation; k_φ and r_l are the lumped dissolution/precipitation rate coefficient and the lumped pore structure index, respectively, and are related to mineral components of the core sample measured by XRD; t is time; m is an exponent of pore surface participation; D is fractal dimension; k_m is dissolution/precipitation rate coefficient; F_s is saturation ratio; C is empirical fractal coefficient; n is the number of hydraulic tubes providing flow through the porous medium; V_b is bulk representative elementary volume; E_a is activation energy; R is gas constant; T is temperature; k_{m25} is dissolution/precipitation rate coefficient at 25°C (298K), enabling the evaluation of the rate constant k_m at any temperature by using k_{25} magnitudes reported elsewhere [72]. Integrating Eqs. (21) and (22) recovers porosity as:

$$\varphi = \left[\varphi_0 + \alpha \nabla \vec{u} + \frac{\alpha - \varphi_0}{K_s}(P - P_0)\right]\left(1 + k_\varphi \varphi_0^r t\right)^{-1/r} \tag{26}$$

Eqs. (10), (11) and (16) give the final governing equations of the model. Finite volume (FV) schemes have been the methods of choice for simulation of flow and transport and porosity is updated each time step. The permeability equation is a modified Kozeny-Carman correlation [73]:

$$k = k_0 \cdot \leq \frac{\varphi^{2m+1}}{(1-\varphi)^2} \frac{(1-\varphi_0)^2}{{\varphi_0}^{2m+1}} \tag{27}$$

where k_0 is initial state of permeability; and m is the cementation index of the formation. The relationship among the pore radius, permeability and porosity can be expressed as [74]:

$$r = \left(\frac{8k\tau}{\varphi}\right)^{1/2} \tag{28}$$

where is τ tortuosity of the porous medium.

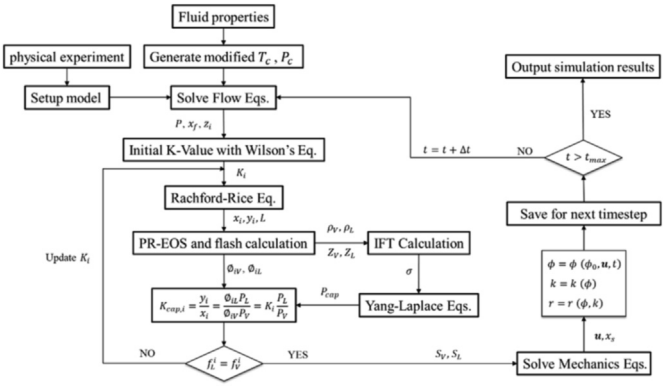

Fig. 2. Coupling procedure in the modified VLE calculation.

The coupling algorithm with a modified VLE calculation procedure is presented in Fig. 2. This work provides a new fully-compositional model to investigate the coupled hydro-mechanical-chemical effect in CO_2 EOR and storage. To overcome the deficiency in convergence speed and calculation efficiency, we substitute the capillary pressure obtained after two-phase flash into compressibility and fugacity calculation before solving equilibrium constant iteratively by successive substitution calculator. In other previously published works, the common practice is to iteratively solve the capillary force each time the equilibrium constant is updated, or iteratively solve the equilibrium constant each time the capillary force is updated [29,75]. Although the previous method and the new algorithm's results are consistent, the computation cost is noteworthy, especially for three-dimensional flow simulations. A small amount of grid increase and refinement will result in a geometrically more extensive computation for the former method than for the latter. Therefore, the cost-effective algorithm makes the framework extendable to simulate flow in a multiscale fracture network by further coupling nature cracks and hydraulic fractures. Constraints in our work are applied by the reservoir's initial pore size distribution recovered from NMR spectroscopy and MIP measurements. A model for the evolution of pore sizes is related to mineralogic composition and lithology constrained by XRD, linking the model's response to the reservoir's key petrophysical properties. These models consider the impact of nanopore-confinement on CO_2 flooding and represent the first attempt to evaluate the safe storage of CO_2 by combining key aspects of phase behavior with the impacts of deformation.

4. Results and discussion

The pore distribution and mineral components are obtained from experiments on cores (NMR and X-ray diffraction) from the Changqing oil field and are used as the basis of a coupled simulation model incorporating geomechanics. Followed by the simulation study of coupled response examining the impacts of confinement, we exhibit the flash calculations and minimum miscible pressure calculations to reveal the phase behavior of CO_2 and crude oil under confined conditions to illustrate the nanopore effect on production CO_2 retention and reservoir deformation.

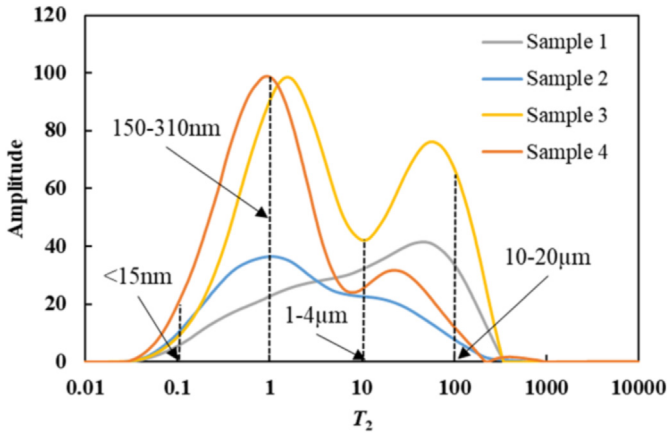

Fig. 3. Pore size distribution of the core samples recovered from the NMR T_2 relaxation time.

4.1. Case study

4.1.1. Pore size distribution and mineral composition

The pore size distribution of the four tight reservoir samples are shown in Fig. 3. The pore diameters vary from less than 15 nm to larger than 20 μm. The pore size distributions of Sample 1 and Sample 2 are relatively uniform, as reflected in the unimodal form of the T_2 spectrum. The peak in the T_2 spectrum of Sample 1 occurs in the short relaxation time region, with diameters in the range 150–310 nm; and the peak of the T_2 spectrum of Sample 2 occurs in the region with a long relaxation time, with diameters of ~4–10 μm. The spectrum for Sample 3 is bimodal, indicating that pore diameters transit nano-scale to micron scale, with the amplitude of the peaks indicating a predominance of pores at the nano-scale. The weakly three-peaked form of the T_2 spectrum for Sample 4, indicates that in addition to many subnanopores and a few micron pores, a small number of cracks may also exist.

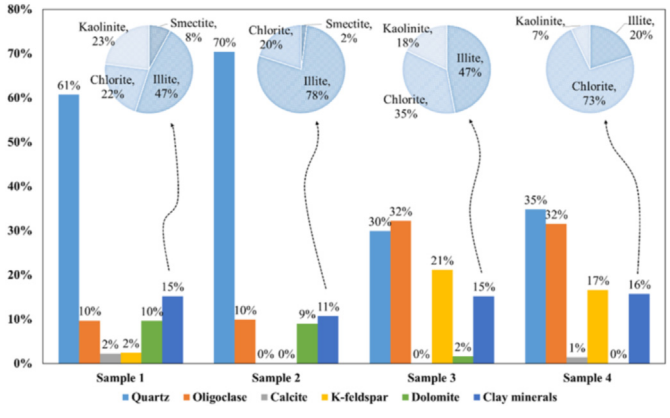

Fig. 4. Mineral constituents of the core samples.

Fig. 4 shows the mineral composition of each of the four samples. The Chang7 layer cores (Sample 1 and Sample 2) have very high quartz content (>60%) with some oligoclase and dolomite. The quartz and oligoclase contents in the Chang8 cores (Sample 3 and Sample 4) are both ~30%, with the next major component of K-feldspar. The clay mineral proportions in the four samples range from 11 to 16%. The Chang7 layer (Sample 1 and Sample 2) is dominated by illite, while the Chang8 layer (Sample 3 and Sample 4) is dominated by chlorite.

Civan et al. [71] fitted the *Carnahan* [76] experimental data to determine $r_l = = 0.81$ and $k_{\varphi 150} = 1.88 \times 10^{-8}$ s^{-1} for quartz at a temperature of 150 °C (432K). Assuming that the values of F_s, C, m, C, r_l, V_b remain unchanged over a range of reservoir conditions, the $k_{\varphi 60}$ of mineral components at 60 °C (333K) can be calculated from Eqs. (24) and (25) according to the $k_{\varphi 150}$ of quartz. Calcite is ignored in the calculation because the calcite content in the four samples is very low. Table 2 shows the values of relevant parameters and calculation results. The lumped parameter k_φ for each sample can be obtained as:

$$k_\varphi = \sum_i^N k_{\varphi 60i} \times M_i \tag{29}$$

where N is the total number of mineral components; M is the percentage of each mineral, the subscript i reperesents the ith mineral component. By substituting M and the calculated value of $k_{\varphi 60}$ in Table 2 into Eq.(29), the average $k_{\varphi 60}$ of the Chang7 layer (Sample 1 and 2) is 2.50×10^{-2} s^{-1}, and the average $k_{\varphi 60}$ of the Chang8 layer (Sample 3 and 4) is 4.31×10^{-3} s^{-1}.

4.1.2. Physical model setup

The model is set with two vertical wells spaced 300 m apart pierce a reservoir where one is a production well with a fixed bottom-hole pressure of 12.25 MPa and the other is an injection well with CO_2 injected at 0.35 m^3/s at surface conditions. Two longitudinal layers with a thickness of 15 m represent the two reservoir units of Chang7 and Chang8. The porosity and permeability distribution of the model are shown in Fig. 5 and Fig. 6.

The geometry of the simulation grid is $20 \times 20 \times 2$, with the two wells located at the 1st and 800th grid blocks, respectively, as detailed in Fig. 7. Zero displacement conditions are set on the base with a pressure of 18.625 MPa imposed on the upper surface. Formation petrophysical parameters are shown in Table 3.

4.1.3. Simulation results of case 1

Prior to modification, the fluid properties and the oil sample composition are shown in Table 4. The data are from the tight oil reservoir of the Changqing oilfield, and is used in the simulation study of Case 1. The components listed are lumped into six pseudo-components, including CO_2, C_1–C_2, C_3–C_4, C_5–C_6, C_7–C_{10}, and C_{11+}, whose critical properties are estimated by Lee-Kesler mixing rules [80].

In this instance, the model with confinement has a higher early production rate (Fig. 8 (a) and (c)) and cumulative production of

Table 2
Parameters and calculation results.

	k_{25} (mol·m^{-2}·s^{-1})	V_m (m^3·mol^{-1})	$k_{m25} = k_{25} \times V_m$ (m·s^{-1})	E_a (J/mol)	k_{m60} (m·s^{-1})	$k_{\varphi 60}$ (s^{-1})
Quartz	1.26×10^{-14} [77]	2.59×10^{-5}	3.26×10^{-19}	8.75×10^4 [77]	1.34×10^{-17}	2.26×10^{-11}
Oligoclase*	3.55×10^{-10} [78]	1.00×10^{-4}	3.55×10^{-14}	5.18×10^4 [78]	3.20×10^{-13}	5.41×10^{-7}
K-feldspar	3.55×10^{-10} [78]	1.09×10^{-4}	3.87×10^{-14}	5.18×10^4 [78]	3.49×10^{-13}	5.90×10^{-7}
Dolomite	1.02×10^{-3} [79]	6.43×10^{-5}	6.56×10^{-8}	2.09×10^4 [79]	1.59×10^{-7}	2.69×10^{-1}

* Albite: Anorthite = 90:10 in Oligoclase.

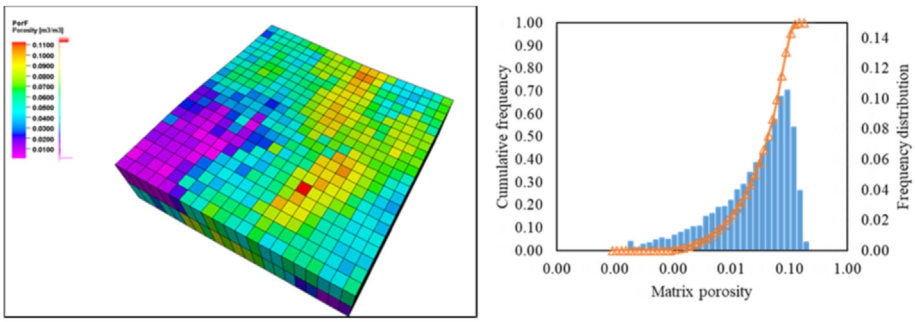

Fig. 5. Heterogeneous porosity model.

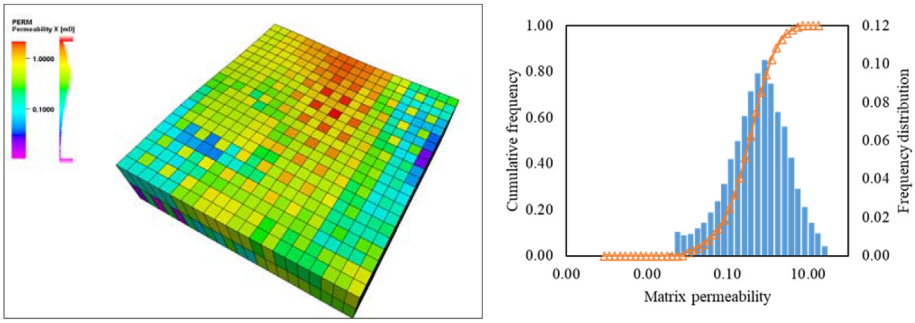

Fig. 6. Heterogeneous permeability model.

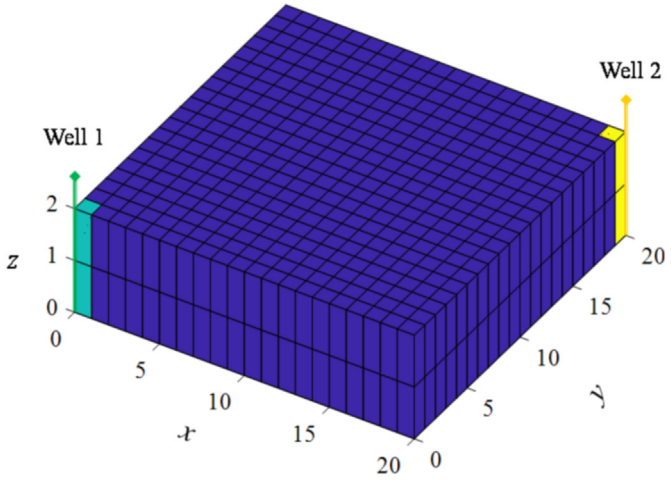

Fig. 7. The numerical model.

lighter and heavier components (Fig. 8 (b) and (d)), which may be caused by the reduction of interfacial tension with miscibility. However, due to the decrease in the flow resistance, CO_2 breakthrough in the production well is more likely and correspondingly will lead to the decline of late-time production. Therefore, it is necessary to mitigate against the early breakthrough of injected CO_2, such as replacing a continuous CO_2 drive by CO_2 WAG.

Subsequently, to eliminate the pressure difference, the injection well is set to 22.5 MPa, and the production well is set to 6 MPa and is shut-in when the gas-oil ratio exceeds 1800 m^3/m^3

Table 3
Petrophysical parameters.

Parameters	Value
Young's module, E	25.80 GPa
Poisson's ratio, θ	0.265
Biot's coefficient, α	0.6
Cementation index, m	2.11
Tortuosity, τ	2.54
Lumped dissolution/precipitation rate coefficient, k_φ	1.88×10^{-8} s^{-1} (Layer 1) 1.44×10^{-6} s^{-1} (Layer 2)
Lumped pore structure index, r_l	0.81
Mean porosity, φ	9.1%
Mean permeability, k	0.77 mD

Table 4
Mole fractions and component characteristics of the crude oil sample (for Case 1).

Comp	Mole fraction	P_c	T_c	a_c	MW	Parachor
CO_2	–	7.376	304.200	0.228	44.010	79.0
CH_4	0.2355	4.600	190.600	0.008	16.535	74.8
C_2H_6	0.0664	4.884	305.400	0.098	30.433	107.7
C_3H_8	0.1056	4.246	369.800	0.152	44.097	151.9
iC_4H_{10}	0.0176	3.648	408.100	0.176	58.124	181.5
nC_4H_{10}	0.0456	3.800	425.200	0.193	58.124	189.6
iC_5H_{12}	0.0232	3.384	460.400	0.227	72.151	225.0
nC_5H_{12}	0.0277	3.374	469.600	0.251	72.151	225.0
C_6	0.0503	3.289	507.500	0.275	86.000	250.1
C_7	0.0286	3.138	543.200	0.308	96.000	278.4
C_8	0.0301	2.951	570.500	0.351	107.000	309.0
C_9	0.0256	2.730	598.500	0.391	121.000	347.2
C_{10}	0.0212	2.534	622.100	0.444	134.000	381.9
C_{11+}	0.3226	2.556	572.013	0.522	266.065	441.0

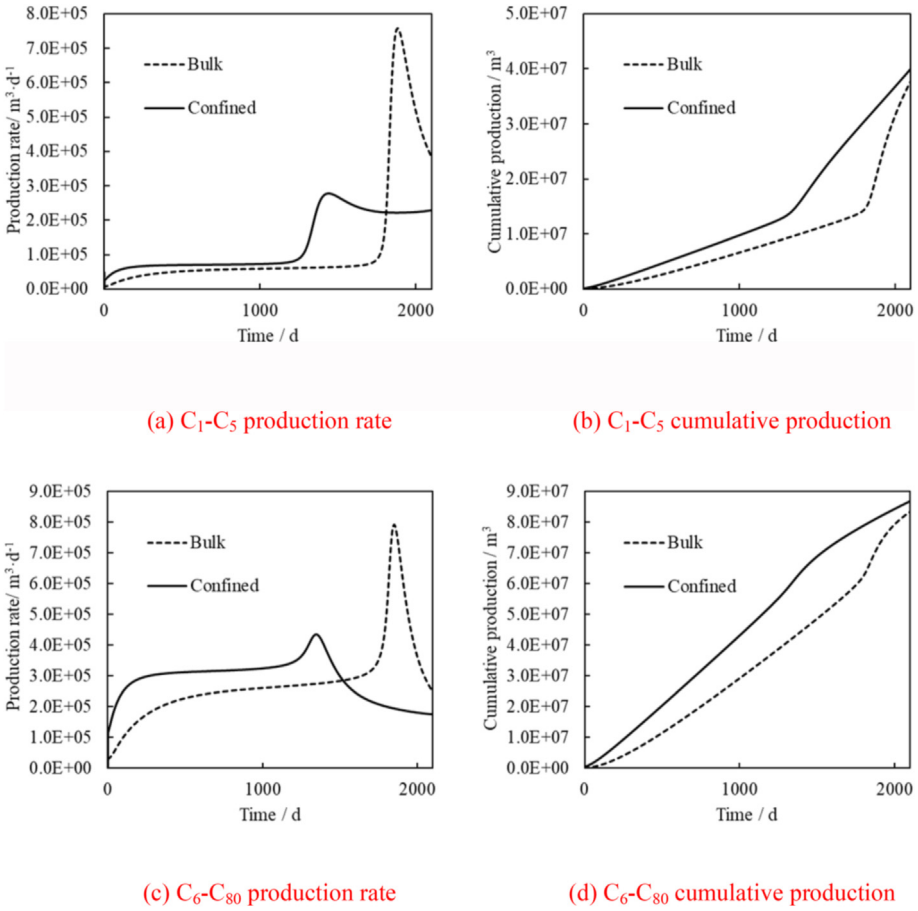

Fig. 8. Production of lighter and heavier components for Case 1.

(approximately 10000 scf/bbl) [81]. The CO_2 retained in the reservoir is the difference between the total injection volume and the total production volume, and the retention rate is the ratio of the retained volume of CO_2 to the total injection volume. The calculation result is shown in Fig. 9. Due to the potential impact of improved CO_2 injection capacity, the model with confinement is shut-in earlier than the model without confinement. With the effects of confinement, production is stopped after 2016 days, the retained volume of CO_2 and retention rate are 1.1 $\times$ 10^8 m^3 and 63.12%, respectively. The model without confinement is shut-in after 3136 days of production; the retained volume of CO_2 and retention rate are 1.04 $\times$ 10^8 m^3 and 60.44%, respectively, both of which are slightly lower than for the model incorporating confinement effects.

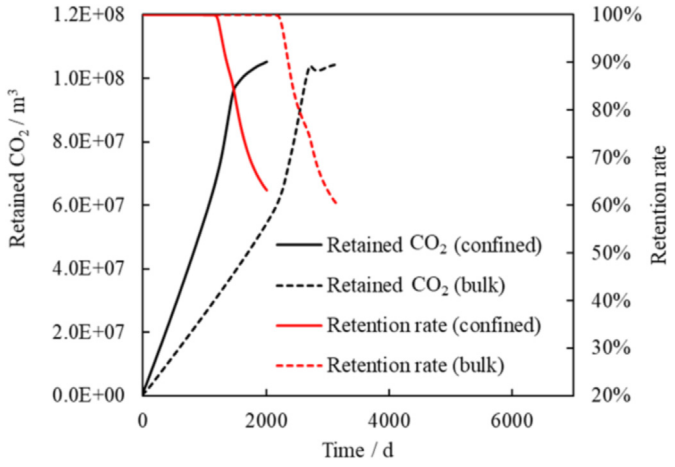

Fig. 9. CO_2 retention for Case 1.

4.2. Impact of confined vapor-liquid equilibrium

To illustrate nano-scale porous media's effect on production and CO_2 retention, we first use the modified PR-EOS to calculate the fugacity coefficient both before and after considering subnanopore confinement. This comparison is shown in Fig. 10 (a) where the dashed line is for bulk fluid the solid line represents the fluid property when confined in the subnanopores (r = 5 nm). The effect of interaction between the fluid and the pore surface on chemical potential may be judged from the fugacity coefficient's deviation [82]. In general, within the range of 300−350K, subnanopore confinement results in the chemical potential of C_3−C_{11+} increasing, and of C_1−C_2 and CO_2 almost unchanged or slightly decreased. Fig. 10 (b) shows that the confinement effect will increase the Z-factor of each component. The Z-factor increases range from ~5% to 35% depending on molar weight and molecular diameter. As Z-factor is directly related to a vapor stream's density, it also affects the flow rate and isothermal compressibility [83]. Therefore, by reducing the pressure, the volume expansion of the fluid in the subnanopores is larger than that of the bulk phase fluid, and this effect is more pronounced for heavy hydrocarbons. Meanwhile, although not obvious, an increase in temperature does result in a reduction in the effect of subnanopore confinement.

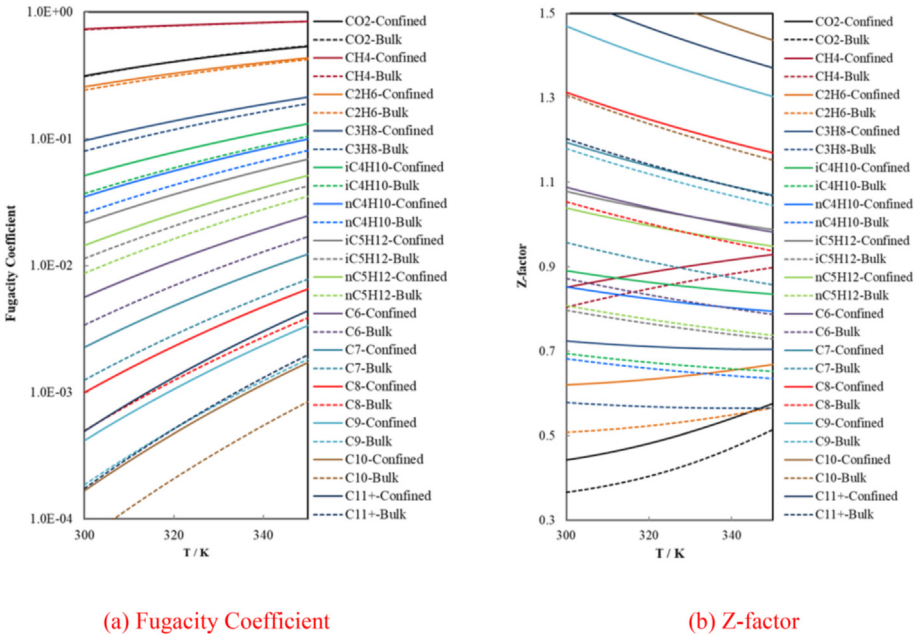

Fig. 10. Shifted fugacity coefficient (a) and Z-factor (b).

CO_2 is mixed with CH_4–C_5H_{12}, C_6–C_{10}, and C_{11+} in 1:4 to calculate the equilibrium K-value of CO_2 at 333K with the change of pressure. The solid lines in Fig. 11 represent properties in the pores at 5 nm, while the dotted lines represent that in the bulk fluid. The nanopores lead to a significant decrease in the CO_2 K-value in the three mixtures. Besides, compared with AA ′(5 nm) and aa ' (Bulk) of the CO_2 K-value curve in the lighter hydrocarbon (CH_4–C_5H_{12}), point A is significantly shifted to the left from point a. This demonstrates that at high-pressure, the escaping pressure of vapor phase CO_2 reduces more significantly in lighter hydrocarbon mixture than that in the heavier mixture. At 4.0 MPa, point A 'is lower than point B′ and point C′, whereas the corresponding point c' in the bulk phase fluid is the highest, indicating that the reduction of pore size leads to the lower ratio of vapor phase CO_2 in the heavier mixture than that in lighter hydrocarbon mixture. It is known that competitive adsorption of molecules and the extraction of CO_2 will cause more heavier hydrocarbons to be bound in the subnanopores. Therefore, if the effect of nanopore restriction is neglected, the CO_2 solubility trapping may be underestimated.

Next, the relative proportions of other hydrocarbon components are kept unchanged, with different mole fractions of CO_2 added to the system. In Fig. 12, the solid line represents the fluid in the 5 nm pores, and the dashed line represents the bulk fluid. The reaction between the fluid molecules and the pore wall results in a significant deviation of the envelope, and the critical point moves in the direction of low pressure and low CO_2 mole fraction. To the left of the critical point, when the system pressure from initial (18.621 MPa), is reduced to below the bubble point pressure (AB), the vapor first appears in the bulk fluid and then in the confined fluid after system pressure continues to drop by ~2 MPa. When system pressure drops from the initial pressure to below the bubble point (A'B'), retrograde condensation can be observed on the right side of the critical point. The liquid first appears in the fractures, then in the subnanopores as the pressure continues to drop. Considering the simultaneous decrease of system pressure and the increase of CO_2 mole fraction (AB′), the vapor first appears in the

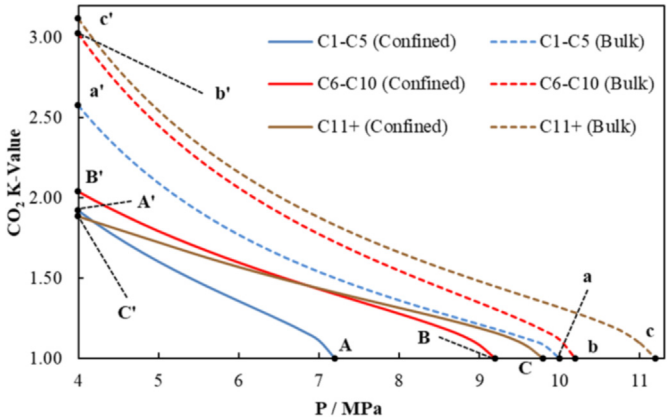

Fig. 11. Comparison of CO_2 K-value in hydrocarbon mixtures for both the confined fluid ($r = 5nm$) and the bulk fluid.

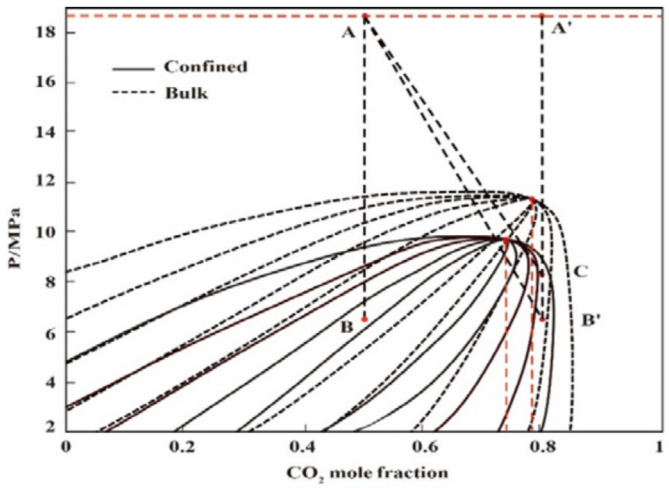

Fig. 12. Comparison of phase envelope for the confined fluid ($r = 5nm$) and the bulk fluid.

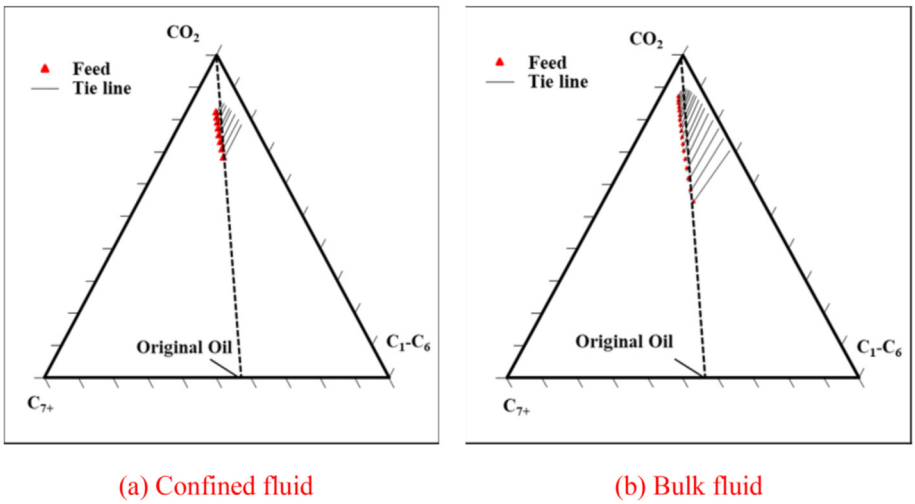

Fig. 13. Multiple contact MMP calculation for both the confined fluid (a) and the bulk fluid (b).

bulk fluid and then in the subnanopores. It is worth noting that for the AC process, retrogressive condensation exists in the subnanopores, but not in the bulk fluid. The comparison between AC and AB′ shows that the influence of the pressure drop rate near the wellbore or the interface between fracture and matrix on the phase state in subnanopores is non-negligible.

4.3. Impact of confined miscibility

The method of Section 3.2 is applied to calculate multiple contact minimum miscible pressures of the oil sample (Case 1) and injected CO_2. In the ternary phase diagram, if the connection between CO_2 and the original oil does not pass through the two-phase region, it can be judged that CO_2 and oil can reach first contact miscibility under the specified pressure. The MMPs of the first contact in the 5 nm pores and bulk fluids are 9.846 and 11.549 MPa. For the calculation process for multiple contact miscibility, in Fig. 13 (a) is the fluid in the 5 nm pore (with multiple contact MMP at 9.142 MPa), and Fig. 13 (b) is for the bulk fluid (with multiple contact MMP at 10.873 MPa). Compared with the bulk fluid, CO_2 concentration in the 5 nm pore is lower when MMP is reached, and the two-phase area is slightly smaller.

Fig. 14 shows the variation of MMP with pore diameter. Recent studies have considered shifted critical properties, and their results show that sub-nanopore confinement causes lower MMPs in unconventional reservoirs but is largely absent in conventional reservoirs - as this effect is only subtle when pore diameters exceed ~10 nm. For this work, lower MMPs are also obtained with nanopore confinement, but the rise in MMPs is significant until the pore diameter exceeds ~100 nm. Besides, in the Bakken, Monterey, Eagle Ford and Niobrara in situ oil samples, the MMPs may increase or decrease when the pore diameter continues to increase [23] indicating that the values of MMP and its trend with the pore diameter are both related to the composition of in situ oil.

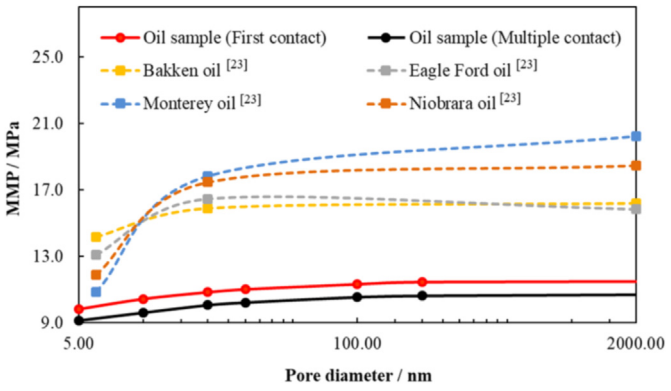

Fig. 14. Sub-nanopore effect on minimum miscible pressure (MMP).

Table 5
Parameters and component properties used in Case 2 [84].

Comp	Mole fraction	P_c	T_c	a_c	MW	Parachor
CO_2	0.0164	7.376	304.200	0.228	44.010	78.000
N_2/CH_4	0.4630	4.580	189.515	0.009	16.159	77.000
C_2H_6—C_5H_{12}	0.2052	4.096	387.607	0.167	45.573	162.633
C_6—C_{13}	0.1911	3.345	597.497	0.386	117.740	378.323
C_{14}—C_{24}	0.0811	1.768	698.515	0.808	248.827	677.873
C_{25}—C_{80}	0.0432	1.169	875.00	1.231	481.520	979.381

Case 2 is conducted for a comparative study considering the effect of composition and MMP. Fluid properties (shown in Table 5) are those from the work of *Mallison* et al. [84]. The MMP and reservoir pressure is 35.75 MPa and 22.5 MPa, respectively.

For the immiscible displacement in Case 2, nanometer pores result in a calculated reduction of initial gas saturation. As a result, the early daily production of components N_2 and C_1—C_5 is lower than the model results without confinement (Fig. 15 (a)). Correspondingly, the early production of components C_6—C_{80} is higher than that of the model without confinement (Fig. 15 (c)). As shown in Fig. 16 and Fig. 17, the CO_2 extraction is impaired in non-obvious ways as pore size decrease in both cases. Although the reduction of lighter components is significant in Case 1 (Fig. 16), the effect extraction on cumulative production is inappreciable compare with miscible displacement. Besides, due to higher light hydrocarbon content for Case 2 (Fig. 17), than the oil of Case 1 (Fig. 16), the production in Case 2 takes less time to reach the shut-in gas-oil ratio (1800 m^3/m^3). The model with and without confinement are shut-in after 1281 and 2324 days, with retention rates of 55.87% and 53.23%, respectively (Fig. 18).

It should be noted that the bottom hole pressure of the injection wells in the two models is quite different in Case 1 affected by miscibility for the model with and without confinement. However, in Case 2, although the model incorporating the effect of confinement has a higher uplift peak, the variations are largely the same.

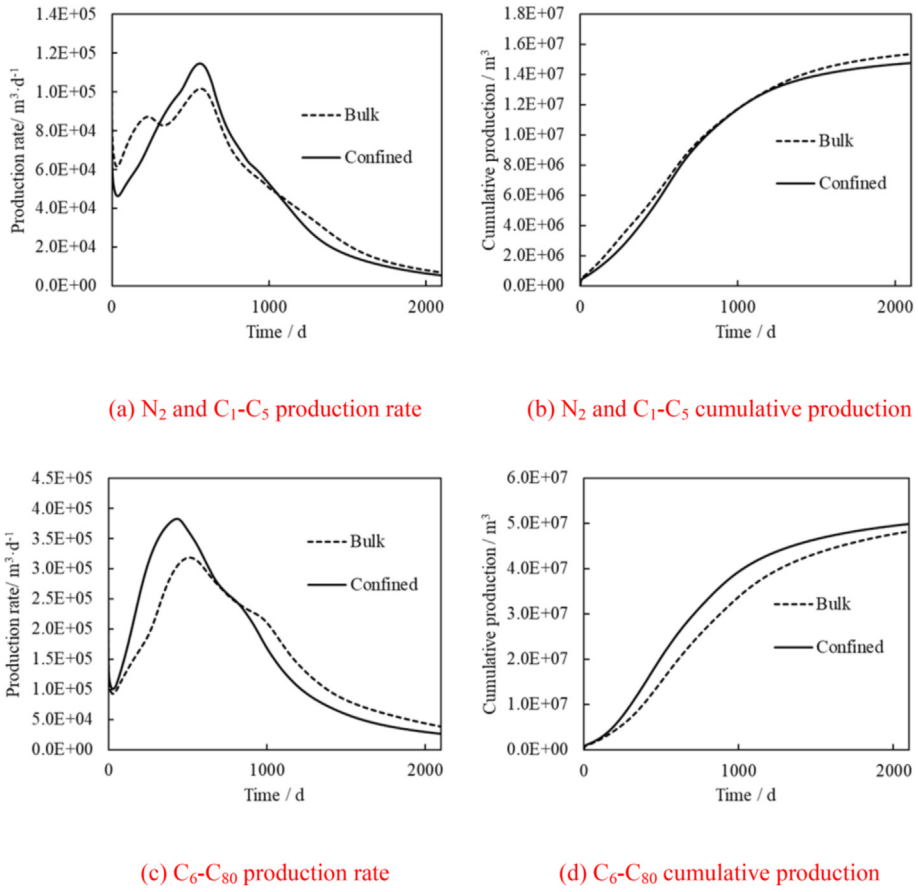

Fig. 15. Production of lighter and heavier components for Case 2.

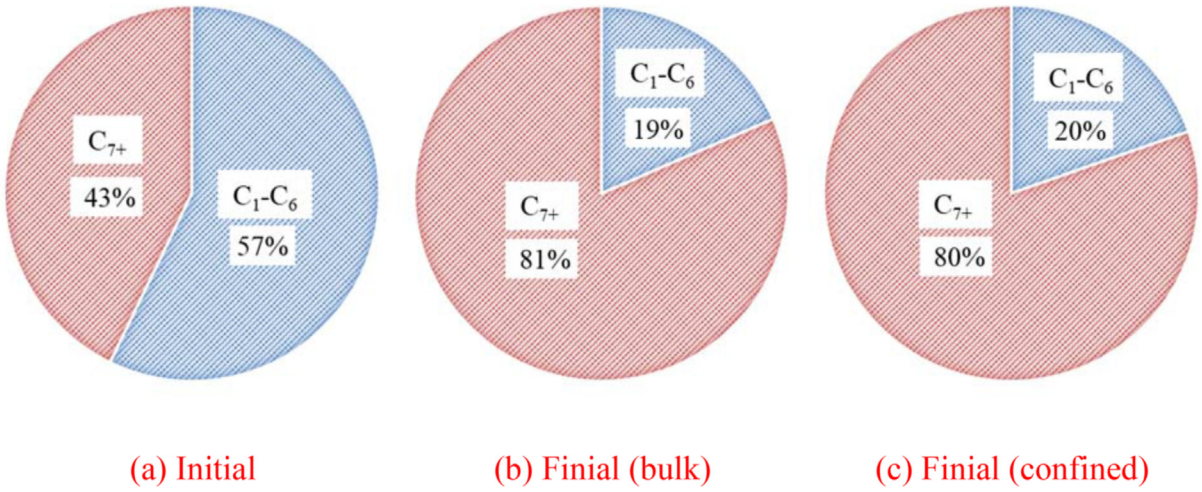

Fig. 16. Comparison of the initial (a) and final (b and c) fluid compositions for Case 1.

Affected by the CO_2 injection rate, the model without confinement exhibits a more significant increase in pore pressure, manifest as more tremendous uplift at the storage site, as shown in Fig. 19 (a). This phenomenon will prompt further discussion on storage safety assessment. As shown in Fig. 20, since CO_2 injection may result in the development or reactivation of any fracture zone near the reservoir and generate substantial microseismic activity [85,86]. Thus, the potential for hydraulic fracturing and fault reactivation must also be examined and discussed in terms of the in-situ stress distribution and geomechanical properties after considering the effect of confinement. This accompanying mechanical evaluation is potentially of relevance to future CCUS operations, especially in devising options for pressure management [90]. Theoretically, due to lower pore pressure and surface uplift, in fact, tight reservoirs may have better long-term capacity and lower risks for large-scale CCS than expected. But a systematic appraisal before injection is

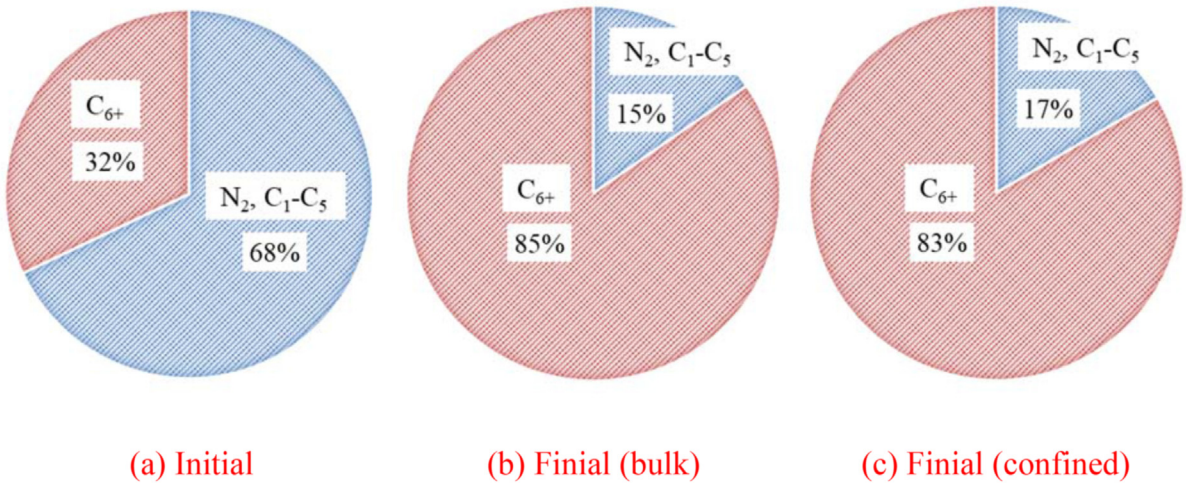

Fig. 17. Comparison of the initial (a) and final (b and c) fluid compositions for Case 2.

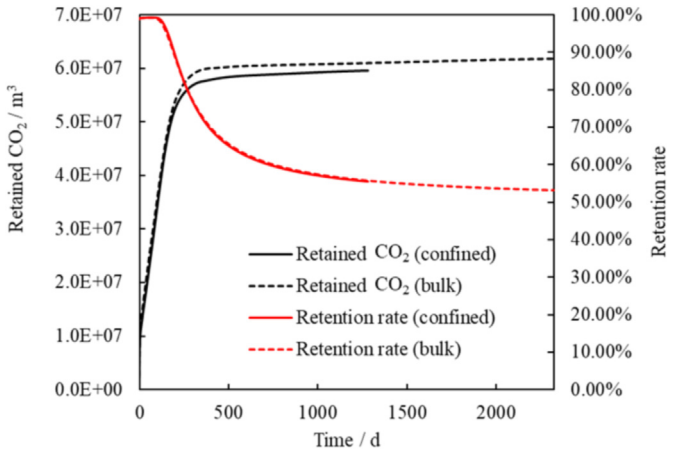

Fig. 18. CO_2 retention for Case 2.

required.

The model established in this work is highly efficient and portable and can deal with large heterogeneity problems. However, the model does not consider CO_2 adsorption, so high adsorbent content (e.g., clay minerals and kerogen) [87,88] may cause significant errors. Moreover, because this approach is a coupled work without temperature effect, it is not suitable for dealing with stress variations (e.g., borehole stability) and asphaltene precipitation (temperature-dominated) around the borehole area as the injected CO_2 temperature is often lower than the reservoir temperature. The model is recommended for sandstone reservoirs with high quartz, feldspar, and calcium content considering the approximation and the neglected effects. The simulation results can be adopted in the formation far from the borehole area, where the temperature variation can be neglected in each horizontal layer. More extensive discussions regarding adsorption/desorption, precipitation kinetics, thermal effect during CO_2 injection and diffusion will be addressed in future work.

5. Conclusions

In this work, a coupled hydro-mechanical-chemical model is established to explore the phase behavior response to sub-nano and to nanopore confinement and its impact on multi-component flow, CO_2 capture and storage safety. The sensitivity analysis of

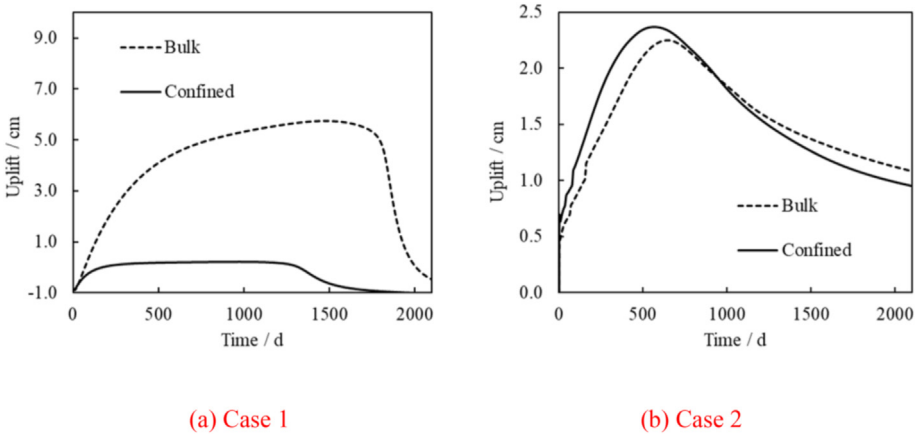

Fig. 19. Uplift of top cells.

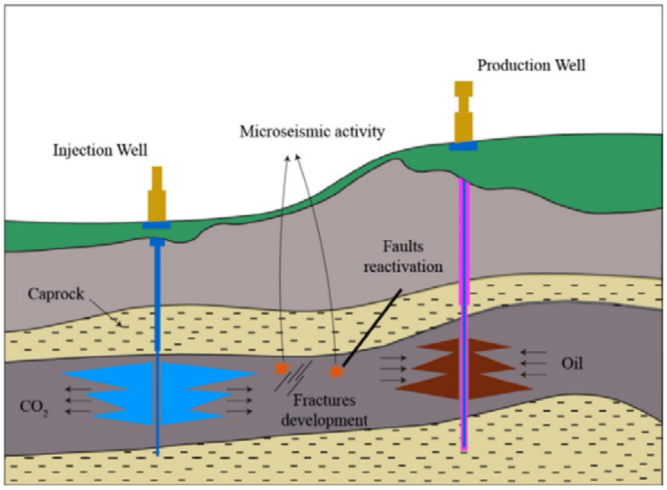

Fig. 20. Schematic diagram of CO_2 sequestion in reservoir.

VLE and miscibility on oil production, CO_2 retention and reservoir deformation are performed. The following conclusions are drawn:

1. The Z-factor with nano-confinement is ~5%–35% higher than that without confinement, depending on molar weight and molecular diameter. Considering the influence of the Z-factor on isothermal compressibility, the volume expansion of the confined fluid is more significant than that of the bulk fluid for a decrease in pressure.
2. At 4 MPa, the K-values of CO_2 in confined light (C_1–C_5), intermediate (C_6- The K-value of CO_2 in hydrocarbon components decreases in nanopores under the same temperature and pressure conditions relative to that for the bulk fluid C_{10}) and heavy(C_{11+}) components in nanopore (5 nm) are 1.92, 2.04 and 1.89, while the corresponding values in the bulk fluid are 2.58, 3.03 and 3.12, respectively. Thus, ignoring the impacts of confinement may underestimate the potential for CO_2 solubility trapping.
3. The nanopore effect can result in a reduction of 1.73 MPa of the MMP between CO_2 and the oil sample in Case 1. Therefore, the confinement effect will promote miscibility, thus increasing the production of each component. However, the nanopore effect on production is virtually unnoticeable for the fluids with the MMP much larger than the reservoir pressure (in Case 2).
4. Lighter components in the produced fluids are reduced sharply compared with the initial proportion due to CO_2 extraction. Multiple contact, extraction, and the consequential miscibility of CO_2 with in-situ oil is the primary mechanism for enhancing oil recovery when reservoir pressure is close to or exceeds the MMP. CO_2 extraction is impaired in non-obvious ways as pore size decreases.
5. The reservoir deformation induced by CO_2 injection may be significantly reduced by the confining effect depending on oil composition and properties. Such deformation will potentially affect CCS risk assessment and the operation of pressure management.

Credit roles

Mingyu Cai: Data curation, Methodology, Writing – original draft. Yuliang Su: Supervision. Derek Elsworth: Supervision, Writing -review & editing. Lei li: Investigation, experiments. Liyao Fan: Investigation, experiments.

Declaration of competing interest

The authors declare that they have no known competing financial interests or personal relationships that could have appeared to influence the work reported in this paper.

Acknowledgements

This project was supported by the National Natural Science Foundation of China (No. 51974348, 51904324), the Graduate Innovative Engineering Project of China University of Petroleum (No. YCX2018017).

References

[1] Yu W, Sepehrnoori K. Chapter 8 - CO2 injection for enhanced oil recovery in tight oil reservoirs. In: Yu W, Sepehrnoori K, editors. Shale gas and tight oil reservoir simulation. Gulf Professional Publishing; 2018. p. 333–76.
[2] Fic J, Pedersen PK. Reservoir characterization of a "tight" oil reservoir, the middle jurassic upper shaunavon member in the whitemud and eastbrook pools, SW saskatchewan. Mar Petrol Geol 2013;44:41–59.
[3] Zhang Q, Wang W-D, Kade Y, Wang B-T, Xiong L. Analysis of gas transport behavior in organic and inorganic nanopores based on a unified apparent gas permeability model. Petrol Sci 2020;17(1):168–81.
[4] Jin L, Hawthorne S, Sorensen J, Pekot L, Kurz B, Smith S, et al. Advancing CO2 enhanced oil recovery and storage in unconventional oil play—experimental studies on Bakken shales. Appl Energy 2017;208:171–83.
[5] Wang L, Tian Y, Yu X, Wang C, Yao B, Wang S, et al. Advances in improved/enhanced oil recovery technologies for tight and shale reservoirs. Fuel 2017;210:425–45.
[6] Aminu MD, Nabavi SA, Rochelle CA, Manovic V. A review of developments in carbon dioxide storage. Appl Energy 2017;208:1389–419.
[7] Ren B, Ren S, Zhang L, Chen G, Zhang H. Monitoring on CO2 migration in a tight oil reservoir during CCS-EOR in Jilin Oilfield China. Energy 2016;98:108–21.
[8] Ren B, Duncan IJ. Reservoir simulation of carbon storage associated with CO2 EOR in residual oil zones, San Andres formation of West Texas, Permian Basin, USA. Energy 2019;167:391–401.
[9] Verdon JP, Kendall J-M, Stork AL, Chadwick RA, White DJ, Bissell RC. Comparison of geomechanical deformation induced by megatonne-scale CO2 storage at Sleipner, Weyburn, and in Salah. Proc Natl Acad Sci Unit States Am 2013;110(30):E2762–71.
[10] Jiang K, Ashworth P, Zhang S, Liang X, Sun Y, Angus D. China's carbon capture, utilization and storage (CCUS) policy: a critical review. Renew Sustain Energy Rev 2020;119:109601.
[11] Wei B, Zhang X, Liu J, Xu X, Pu W, Bai M. Adsorptive behaviors of supercritical CO2 in tight porous media and triggered chemical reactions with rock minerals during CO2-EOR and-sequestration. Chem Eng J 2020;381:122577.
[12] Hasan MMF, First EL, Boukouvala F, Floudas CA. A multi-scale framework for CO2 capture, utilization, and sequestration: CCUS and CCU. Comput Chem Eng 2015;81:2–21.
[13] Bachu S. Identification of oil reservoirs suitable for CO2-EOR and CO2 storage (CCUS) using reserves databases, with application to Alberta, Canada. Int J Greenh Gas Control 2016;44:152–65.
[14] Chen B, Pawar RJ. Characterization of CO2 storage and enhanced oil recovery in residual oil zones. Energy 2019;183:291–304.
[15] Deroche I, Daou TJ, Picard C, Coasne B. Reminiscent capillarity in sub-nanopores. Nat Commun 2019;10(1):1–10.
[16] Liu X, Zhang D. A review of phase behavior simulation of hydrocarbons in confined space: implications for shale oil and shale gas. J Nat Gas Sci Eng 2019:102901.
[17] Wang D, Yao J, Chen Z, Song W, Sun H. Multiphase flow model from pores to cores in organic-rich shale. J Petrol Sci Eng 2020:107317.
[18] Song W, Yao J, Ma J, Sun H, Li Y, Yang Y, et al. Numerical simulation of multiphase flow in nanoporous organic matter with application to coal and gas shale systems. Water Resour Res 2018;54(2):1077–92.
[19] Coasne B, Galarneau A, Pellenq RJM, Di Renzo F. Adsorption, intrusion and freezing in porous silica: the view from the nanoscale. Chem Soc Rev 2013;42(9):4141–71.
[20] Jin B, Bi R, Nasrabadi H. Molecular simulation of the pore size distribution effect on phase behavior of methane confined in nanopores. Fluid Phase Equil 2017;452:94–102.
[21] Salahshoor S, Fahes M, Teodoriu C. A review on the effect of confinement on phase behavior in tight formations. J Nat Gas Sci Eng 2018;51:89–103.
[22] Zhang K, Jia N, Li S. Exploring the effects of four important factors on oil–CO 2 interfacial properties and miscibility in nanopores. RSC Adv 2017;7(85):54164–77.
[23] Teklu TW, Alharthy N, Kazemi H, Yin X, Graves RM. Hydrocarbon and non-hydrocarbon gas miscibility with light oil in shale reservoirs. Conference Hydrocarbon and non-hydrocarbon gas miscibility with light oil in shale

reservoirs. Society of Petroleum Engineers.
[24] Song W, Liu L, Wang D, Li Y, Prodanović M, Yao J. Nanoscale confined multicomponent hydrocarbon thermodynamic phase behavior and multiphase transport ability in nanoporous material. Chem Eng J 2020;382:122974.
[25] Zhang K, Jia N, Liu L. CO2 storage in fractured nanopores underground: phase behaviour study. Appl Energy 2019;238:911–28.
[26] Lijun L, Jun Y, Hai S, Zhaoqin H, Xia Y, Longlong L. Compositional modeling of shale condensate gas flow with multiple transport mechanisms. J Petrol Sci Eng 2019;172:1186–201.
[27] Zhang Y, Yu W, Li Z, Sepehrnoori K. Simulation study of factors affecting CO2 Huff-n-Puff process in tight oil reservoirs. J Petrol Sci Eng 2018;163:264–9.
[28] Nojabaei B, Johns RT, Chu L. Effect of capillary pressure on phase behavior in tight rocks and shales. SPE Reservoir Eval Eng 2013;16:281–9. 03.
[29] Li L, Sheng JJ. Nanopore confinement effects on phase behavior and capillary pressure in a Wolfcamp shale reservoir. J Taiwan Inst Chem Eng 2017;78:317–28.
[30] Tian Y, Xiong Y, Wang L, Lei Z, Zhang Y, Yin X, et al. A compositional model for gas injection IOR/EOR in tight oil reservoirs under coupled nanopore confinement and geomechanics effects. J Nat Gas Sci Eng 2019;71:102973.
[31] Zhang N, Zhao F, Guo P, Li J, Gong W, Guo Z, et al. Nanoscale pore structure characterization and permeability of mudrocks and fine-grained sandstones in coal reservoirs by scanning electron microscopy, mercury intrusion porosimetry, and low-field nuclear magnetic resonance. Geofluids. 2018 2018:2905141.
[32] Chen Z, Liu J, Elsworth D, Connell LD, Pan Z. Impact of CO2 injection and differential deformation on CO2 injectivity under in-situ stress conditions. Int J Coal Geol 2010;81(2):97–108.
[33] Hangx S, van der Linden A, Marcelis F, Bauer A. The effect of CO2 on the mechanical properties of the Captain Sandstone: geological storage of CO2 at the Goldeneye field (UK). Int J Greenh Gas Control 2013;19:609–19.
[34] Sheng G, Zhao H, Su Y, Javadpour F, Wang C, Zhou Y, et al. An analytical model to couple gas storage and transport capacity in organic matter with noncircular pores. Fuel 2020;268:117288.
[35] Cai J, Li C, Song K, Zou S, Yang Z, Shen Y, et al. The influence of salinity and mineral components on spontaneous imbibition in tight sandstone. Fuel 2020;269:117087.
[36] Fan C, Elsworth D, Li S, Zhou L, Yang Z, Song Y. Thermo-hydro-mechanical-chemical couplings controlling CH4 production and CO2 sequestration in enhanced coalbed methane recovery. Energy 2019;173:1054–77.
[37] Zhang X, Wei B, Shang J, Gao K, Pu W, Xu X, et al. Alterations of geochemical properties of a tight sandstone reservoir caused by supercritical CO2-brine-rock interactions in CO2-EOR and geosequestration. J CO2 Util. 2018;28:408–18.
[38] Luquot L, Gouze P, Niemi A, Bensabat J, Carrera J. CO2-rich brine percolation experiments through Heletz reservoir rock samples (Israel): role of the flow rate and brine composition. Int J Greenh Gas Control 2016;48:44–58.
[39] Liu P, Zhang T, Sun S. A tutorial review of reactive transport modeling and risk assessment for geologic CO2 sequestration. Comput Geosci 2019.
[40] Emmanuel S, Berkowitz B. Mixing-induced precipitation and porosity evolution in porous media. Adv Water Resour 2005;28(4):337–44.
[41] Stephens JC, Hering JG. Factors affecting the dissolution kinetics of volcanic ash soils: dependencies on pH, CO2, and oxalate. Appl Geochem 2004;19(8):1217–32.
[42] Rosenbauer RJ, Koksalan T, Palandri JL. Experimental investigation of CO2–brine–rock interactions at elevated temperature and pressure: implications for CO2 sequestration in deep-saline aquifers. Fuel Process Technol 2005;86(14–15):1581–97.
[43] Smith MM, Sholokhova Y, Hao Y, Carroll SA. Evaporite caprock integrity: an experimental study of reactive mineralogy and pore-scale heterogeneity during brine-CO2 exposure. Environ Sci Technol 2013;47(1):262–8.
[44] Cui G, Wang Y, Rui Z, Chen B, Ren S, Zhang L. Assessing the combined influence of fluid-rock interactions on reservoir properties and injectivity during CO2 storage in saline aquifers. Energy 2018;155:281–96.
[45] Bemani A, Baghban A, Mohammadi AH, Andersen PØ. Estimation of adsorption capacity of CO2, CH4, and their binary mixtures in Quidam shale using LSSVM: application in CO2 enhanced shale gas recovery and CO2 storage. J Nat Gas Sci Eng 2020;76:103204.
[46] Kazemi M, Takbiri-Borujeni A. Molecular dynamics study of carbon dioxide storage in carbon-based organic nanopores. SPE annual technical conference and exhibition. Dubai, UAE: Society of Petroleum Engineers; 2016. p. 10.
[47] Zhou J, Jin Z, Luo KH. The role of brine in gas adsorption and dissolution in kerogen nanopores for enhanced gas recovery and CO2 sequestration. Chem Eng J 2020;399:125704.
[48] Yan B, Wang Y, Killough JE. A fully compositional model considering the effect of nanopores in tight oil reservoirs. J Petrol Sci Eng 2017;152:675–82.
[49] Fakcharoenphol P, Xiong Y, Hu L, Winterfeld PH, Xu T, Wu Y-S. User's guide of TOUGH2-EGS. A coupled geomechanical and reactive geochemical simulator for fluid and heat flow in enhanced geothermal systems version 1.0. Golden, CO (United States): Colorado School of Mines; 2013.
[50] Chen S, Ding B, Gong L, Huang Z, Yu B, Sun S. Comparison of multi-field coupling numerical simulation in hot dry rock thermal exploitation of enhanced geothermal systems. 2020.
[51] Xu H, Fan Y, Hu F, Li C, Yu J, Liu Z, et al. Characterization of pore throat size distribution in tight sandstones with nuclear magnetic resonance and high-pressure mercury intrusion. Energies 2019;12(8):1528.
[52] Pearce JK, Dawson GKW, Golab A, Knuefing L, Sommacal S, Rudolph V, et al. A combined geochemical and μCT study on the CO2 reactivity of Surat Basin reservoir and cap-rock cores: porosity changes, mineral dissolution and fines migration. Int J Greenh Gas Control 2019;80:10–24.
[53] Alharthy N, Nguyen T, Teklul T, Kazemil H, Graves R. Multiphase compositional modeling in small-scale pores of unconventional shale reservoirs: paper presented at SPE Annual Technical Conference and Exhibition. New Orleans: Louisiana; September. 2013.
[54] Sherafati M, Jessen K. Stability analysis for multicomponent mixtures including capillary pressure. Fluid Phase Equil 2017;433:56–66.
[55] Zarragoicoechea G, Kuz V. Van der Waals equation of state for a fluid in a nanopore. Phys Rev E 2002;65:021110.
[56] Teklu TW, Alharthy N, Kazemi H, Yin X, Graves RM, AlSumaiti AM. Phase behavior and minimum miscibility pressure in nanopores. SPE Reservoir Eval Eng 2014;17:396–403. 03.
[57] Singh SK, Sinha A, Deo G, Singh JK. Vapor–Liquid phase coexistence, critical properties, and surface tension of confined alkanes. J Phys Chem C 2009;113(17):7170–80.
[58] Devegowda D, Sapmanee K, Civan F, Sigal RF. Phase behavior of gas condensates in shales due to pore proximity effects: implications for transport, reserves and well productivity. Conference Phase behavior of gas condensates in shales due to pore proximity effects: implications for transport, reserves and well productivity. Society of Petroleum Engineers.
[59] Ma Y, Jin L, Jamili A. Modifying van der Waals equation of state to consider influence of confinement on phase behavior. SPE annual technical conference and exhibition. New Orleans, Louisiana, USA: Society of Petroleum Engineers; 2013. p. 12.
[60] Yu W, Zhang Y, Varavei A, Sepehrnoori K, Zhang T, Wu K, et al. Compositional simulation of CO 2 Huff'n'Puff in Eagle Ford tight oil reservoirs with CO 2 molecular diffusion, nanopore confinement, and complex natural fractures. SPE Reservoir Eval Eng 2019.
[61] Ahmadi K, Johns RT. Multiple-mixing-cell method for MMP calculations. SPE J 2011;16:733–42. 04.
[62] Pederson K, Fjellerup J, Thomassen P, Fredenslund A. Studies of gas injection into oil reservoirs by a cell-to-cell simulation model. Conference Studies of gas injection into oil reservoirs by a cell-to-cell simulation model. Society of Petroleum Engineers.
[63] Zeng Q, Yao J, Shao J. An extended finite element solution for hydraulic fracturing with thermo-hydro-elastic–plastic coupling. Comput Methods Appl Mech Eng 2020;364:112967.
[64] Sheng G, Su Y, Wang W. A new fractal approach for describing induced-fracture porosity/permeability/compressibility in stimulated unconventional reservoirs. J Petrol Sci Eng 2019;179:855–66.
[65] Wang L, Chen Z, Wang C, Elsworth D, Liu W. Reassessment of coal permeability evolution using steady-state flow methods: the role of flow regime transition. Int J Coal Geol 2019;211:103210.
[66] Cai J, Hu X. Petrophysical characterization and fluids transport in unconventional reservoirs. Elsevier; 2019.
[67] Haagenson R, Rajaram H, Allen J. A generalized poroelastic model using FEniCS with insights into the Noordbergum effect. Comput Geosci 2020;135:104399.
[68] Andersen O, Nilsen HM, Raynaud X. Coupled geomechanics and flow simulation on corner-point and polyhedral grids. Conference coupled geomechanics and flow simulation on corner-point and polyhedral grids. Society of Petroleum Engineers.
[69] Zeng Q-D, Yao J, Shao J. Study of hydraulic fracturing in an anisotropic poroelastic medium via a hybrid EDFM-XFEM approach. Comput Geotech 2019;105:51–68.
[70] Ingham DB, Pop I. Transport phenomena in porous media. Elsevier; 1998.
[71] Civan F. Scale effect on porosity and permeability: kinetics, model, and correlation. AIChE J 2001;47(2):271–87.
[72] Xu T, Apps JA, Pruess K. Mineral sequestration of carbon dioxide in a sandstone–shale system. Chem Geol 2005;217(3–4):295–318.
[73] Carman PC. Fluid flow through granular beds. Trans Inst Chem Eng 1937;15:150–66.
[74] Civan F, Devegowda D, Sigal RF. Critical evaluation and improvement of methods for determination of matrix permeability of shale. Conference Critical evaluation and improvement of methods for determination of matrix permeability of shale. Society of Petroleum Engineers.
[75] Yang G, Chai D, Fan Z, Li X. Capillary condensation of single- and multicomponent fluids in nanopores. Ind Eng Chem Res 2019;58(41):19302–15.
[76] Carnahan C. Coupling of precipitation/dissolution reactions to mass diffusion. CA (USA): Lawrence Berkeley Lab.; 1988.
[77] Tester JW, Worley WG, Robinson BA, Grigsby CO, Feerer JL. Correlating quartz dissolution kinetics in pure water from 25 to 625°C. Geochem Cosmochim Acta 1994;58(11):2407–20.
[78] Alex EB, Lisa LS. Chapter 7. FELDSPAR DISSOLUTION KINETICS. Berlin, Boston: De Gruyter; 1995. p. 291–352.
[79] Gautelier M, Oelkers EH, Schott J. An experimental study of dolomite dissolution rates as a function of pH from− 0.5 to 5 and temperature from 25 to 80 C. Chem Geol 1999;157(1–2):13–26.
[80] Lee BI, Kesler MG. A generalized thermodynamic correlation based on three-parameter corresponding states. AIChE J 1975;21(3):510–27.
[81] Brock WR, Bryan LA. Summary results of CO2 EOR field tests, 1972-1987. Low permeability reservoirs symposium. Denver, Colorado: Society of Petroleum

Engineers; 1989. p. 10.
[82] Walas SM. Phase equilibria in chemical engineering. Butterworth-Heinemann; 2013.
[83] Gaganis V, Homouz D, Maalouf M, Khoury N, Polychronopoulou K. An efficient method to predict compressibility factor of natural gas streams. Energies 2019;12(13):2577.
[84] Mallison BT, Gerritsen MG, Jessen K, Orr FM. High order upwind schemes for two-phase, multicomponent flow. SPE J 2005;10:297–311. 03.
[85] Elsworth D, Im K, Fang Y, Ishibashi T, Wang C. Induced seismicity and permeability evolution in gas shales, CO2 storage and deep geothermal energy. Conference induced seismicity and permeability evolution in gas shales, CO2 storage and deep geothermal energy, Singapore. Springer Singapore, p. 1-20.
[86] Zhang L, Zhang S, Jiang W, Wang Z, Li J, Bian Y. A mechanism of fluid exchange associated to CO2 leakage along activated fault during geologic storage. Energy 2018;165:1178–90.
[87] Fakher S, Abdelaal H, Elgahawy Y, El-Tonbary A. A review of long-term carbon dioxide storage in shale reservoirs. Conference A review of long-term carbon dioxide storage in shale reservoirs, vol. Day 2 tue, july 21. 2020.
[88] Al-Arfaj MK. Adsorption potential analysis for shale and pure clay samples: an experimental study. In: Conference adsorption potential analysis for shale and pure clay samples: an experimental study, vol. Day 3 wed, july 22; 2020.
[89] Zhang L, Wang Y, Miao X, Gan M, Li X. Geochemistry in geologic CO2 utilization and storage: a brief review. Adv Geo-Energy Res 2019;3(3):304–13.
[90] Singh H. Impact of four different CO2 injection schemes on extent of reservoir pressure and saturation. Adv Geo-Energy Res 2018;2(3):305–18.